

## Using a Low-Order Model to Detect and Characterize Tornadoes in Multiple-Doppler Radar Data

COREY K. POTVIN AND ALAN SHAPIRO

*School of Meteorology, and Center for Analysis and Prediction of Storms, University of Oklahoma, Norman, Oklahoma*

TIAN-YOU YU

*School of Electrical and Computer Engineering, University of Oklahoma, Norman, Oklahoma*

JIDONG GAO

*Center for Analysis and Prediction of Storms, University of Oklahoma, Norman, Oklahoma*

MING XUE

*School of Meteorology, and Center for Analysis and Prediction of Storms, University of Oklahoma, Norman, Oklahoma*

(Manuscript received 1 November 2007, in final form 1 August 2008)

### ABSTRACT

A new multiple-Doppler radar analysis technique is presented for the objective detection and characterization of tornado-like vortices. The technique consists of fitting radial wind data from two or more radars to a simple analytical model of a vortex and its near-environment. The model combines a uniform flow, linear shear flow, linear divergence flow (all of which compose a broadscale flow), and a modified combined Rankine vortex (representing the tornado). The vortex and its environment are allowed to translate. The parameters in the low-order model are determined by minimizing a cost function that accounts for the discrepancy between the model and observed radial winds. Since vortex translation is taken into account, the cost function can be evaluated over time as well as space, and thus the observations can be used at the actual times and locations where they were acquired. The technique is first tested using analytically simulated observations whose wind field and error characteristics are systematically varied. An Advanced Regional Prediction System (ARPS) high-resolution numerical simulation of a supercell and associated tornado is then used to emulate an observation dataset. The method is tested with two virtual radars for several radar-sampling strategies. Finally, the technique is applied to a dataset of real dual-Doppler observations of a tornado that struck central Oklahoma on 8 May 2003. The method shows skill in retrieving the tornado path and radar-grid-scale features of the horizontal wind field in the vicinity of the tornado. The best results are obtained using a two-step procedure in which the broadscale flow is retrieved first.

### 1. Introduction

A major focus in severe weather research for operational applications is the development of robust techniques to detect mesocyclones and tornadoes in real time. Several factors limit the success of such techniques. A significant portion of the lower troposphere, within which tornadoes and low-level mesocyclones occur, is

unobserved by the current Weather Surveillance Radar-1988 Doppler (WSR-88D) network (Maddox et al. 2002). This lack of coverage is primarily due to the large spacing, about 230 km, between radars and the increase of radar beam height above ground with range due to both the nonzero beam elevation and the earth curvature effect. In addition, the degradation of azimuthal resolution with distance from the radar limits our ability to observe finescale features of significant circulations that do occur within the WSR-88D domain. Finally, the nearly complete lack of overlapping operational radar coverage at low levels prevents the application of multiple-Doppler techniques.

---

*Corresponding author address:* Corey K. Potvin, School of Meteorology, University of Oklahoma, 120 David L. Boren Blvd., Norman, OK 73072.  
E-mail: corey.potvin@ou.edu

The National Science Foundation (NSF) Collaborative Adaptive Sensing of the Atmosphere (CASA) Engineering Research Center is exploring the feasibility of a nationwide network of low-cost, low-power, densely spaced X-band radars that would reduce the gaps in spatial coverage of the current WSR-88D system (McLaughlin et al. 2005). These radars would adaptively scan the lower troposphere based on a variety of end-user interests, including the forecaster's need to focus on severe and hazardous meteorological phenomena such as thunderstorms and regions of rotation. A test bed of four CASA radars [Integrative Project One (IP1); Brotzge et al. 2007]] has been deployed in Oklahoma. These radars have a half-power beamwidth and gate spacing of  $1.8^\circ$  and 26 m, respectively. The method presented herein is designed to utilize the increased radar data resolution and coverage provided by a CASA-like network to detect and characterize tornadoes using a new multiple-Doppler vortex retrieval technique.

Multiple-Doppler wind retrieval techniques take advantage of the additional information gained by sampling a wind field from more than one radar perspective. Dual-Doppler wind analyses have proven vital in advancing our understanding of boundary layer and severe convection phenomena (Shapiro and Mewes 1999 and references therein). Traditional methods consider the geometrical relation between the vector wind field and the radial wind components from two or more scanning radars, possibly augmented by the mass conservation equation. Though the technique presented herein also uses radial velocity observations from multiple radars, only the parameters describing the spatial structure of a low-order vortex model (described in section 2) are sought.

Wind retrieval methods typically use weak (approximately satisfied, in a least squares error sense) or strong (exactly satisfied) equation constraints in addition to single- or multiple-Doppler data to variationally adjust the analysis field. Three-dimensional variational data assimilation (3DVAR) wind analysis methods include that of Gao et al. (1999), which incorporates an analysis background and imposes mass continuity as a weak constraint. The four-dimensional variational data assimilation (4DVAR) method obtains an initial model state that minimizes the discrepancy between model-predicted fields and observations (and usually also background fields) over a time window. Sophisticated applications of this method use a full set of numerical weather prediction equations (Sun et al. 1991; Kapitza 1991; Sun and Crook 1994, 2001).

In addition to the generic methods discussed above, single- and dual-Doppler techniques have been devel-

oped to retrieve the three-dimensional velocity field of a specific class of meteorologically significant flows: intense vortices. These techniques fit radial velocity data to a vortex model in order to recover key characteristics of the vortex flow. The velocity track display (VTD; Lee et al. 1994) airborne radar data analysis method performs a harmonic analysis of single-Doppler data collected on successive flight legs. In this method, Doppler winds on constant radius (as measured from the tropical cyclone center), constant-altitude rings are decomposed into the tangential, mean radial and mean cross-track components of the horizontal flow. Spatial interpolation is required since observations are not collocated with the analysis rings. In the extended VTD (EVTD; Roux and Marks 1996) technique, Doppler observations from two successive flight legs are considered simultaneously, and data are analyzed at all rings simultaneously for each level. This allows for the wavenumber 1 component of the radial wind to be recovered in addition to the symmetric mean radial wind.

The ground-based VTD (GBVTD; Lee et al. 1999) method was proposed to study the evolution and wind structure of landfalling tropical cyclones. In this technique, a single Doppler radar is situated at the ground, thereby requiring a new geometrical formulation of the VTD-like analysis. Since flight tracks are not necessary for data collection, this method can be used to decompose the wind fields of vortices other than tropical cyclones. Lee and Wurman (2005) used GBVTD to examine the three-dimensional structure of a tornado sampled by a Doppler on Wheels (DOW) radar. Liou et al. (2006) extended the GBVTD method to overlapping data coverage from two radars [i.e., extended GBVTD (EGBVTD)]. This allowed for the radial wind component to be retrieved up to wavenumber 1 structure (as with EVT D), and also improved the accuracy of the recovered tangential wind. This technique was also capable of recovering more of the vortex wind field than traditional dual-Doppler analysis when data are missing.

Dowell et al. (2005) and Wurman and Alexander (2005) used an axisymmetric, translating vortex model to retrieve velocity profiles in a DOW-observed tornado at successive volume-scan times. The model used in the new technique presented herein combines a translating axisymmetric vortex (modified combined Rankine vortex) with several broader-scale flows.

Since the implementation of the WSR-88D network, several algorithms have been developed to aid forecasters in real-time identification of intense small and mesoscale vortices. The National Severe Storms Laboratory (NSSL) Mesocyclone Detection Algorithm (MDA; Stumpf et al. 1998) was designed to alert forecasters to the presence of supercell thunderstorms, which produce a large portion

of tornadoes in the United States. The NSSL Tornado Detection Algorithm (TDA; Mitchell et al. 1998) calculates the azimuthal shear of radial wind using adjacent radar resolution volumes, and identifies regions where shear exceeds a threshold. Multiple thresholds are used to identify circulations on multiple scales. Features can be tracked and, using linear extrapolation, their paths predicted. Unfortunately, the success of the TDA algorithm and others of its kind [e.g., Tornado Vortex Signature (TVS) algorithm; Crum and Alberty (1993)] depends upon the chosen detection thresholds, the suitability of which is largely range and storm dependent. Thus, this approach may be subject to high false-alarm rate or low probability of detection values.

Other algorithms have been developed to identify potentially significant vortices. The linear-least squares derivative (LLSD) technique estimates the derivatives of the radial wind by least squares fitting Doppler velocity observations to a linear spatial model (Smith and Elmore 2004). This method produces more accurate estimates of shear than methods that rely upon point-to-point velocity measurements. Fuzzy-logic approaches (e.g., Wang et al. 2008) acknowledge the typically large overlap between the probability distribution functions of parameters used in vortex detection techniques, as opposed to binary methods that use rigid thresholds to make detection decisions. Liu et al. (2007) proposed a preliminary tornado detection algorithm based on multiscale wavelet analysis of radial velocity data. Finally, neural network methods have been developed that show skill in identifying precursor circulations for tornado genesis (Marzban and Stumpf 1996). This approach also allows the level of confidence in the predicted outcome (tornado or no tornado) to be computed.

In this study, radial wind observations from two or more close-proximity Doppler radars with overlapping domains are fit to an analytical low-order model of a vortex and near environment. The model control parameters include vortex location, size, intensity, and translation velocity. This method is designed to capitalize upon the increased observational density and overlapping coverage of a CASA-like radar network to detect small-scale vortices and also to provide vortex characteristic estimates, which may improve tornado nowcasting. This capability distinguishes our approach from traditional dual-Doppler analysis, which does not constrain the retrieved wind field with a spatial vortex model and thus is not designed to retrieve vortex characteristics. The vortex parameters are obtained by minimizing a cost function that measures the discrepancy between the observed and model radial wind fields. The cost function is defined as an integral over space (volume) and time. By taking the translation of the system

into account, the radar data can be used at their actual locations and times of acquisition.

The paper is organized as follows. The low-order model is introduced in section 2. The computation and minimization of the cost function is described in section 3. The simulation of the observation datasets used to test the technique is described in section 4. The technique is tested against analytically generated observations in section 5, and against a high-resolution Advanced Regional Prediction System (ARPS; Xue et al. 2001) dataset of a tornado vortex and mesocyclone in section 6. Section 7 describes tests using dual-Doppler observations of an F4 tornado that struck central Oklahoma on 8 May 2003. A summary and plans for future work follow in section 8.

## 2. Description of low-order model

The low-order model used in this study comprises four idealized flow fields: a uniform flow, linear shear flow, linear divergence flow, and modified combined Rankine vortex (MCRV; representing the tornado). Our use of the MCRV model is supported qualitatively by high-resolution mobile radar observations of tornadoes whose azimuthally averaged tangential winds roughly followed this profile (Wurman and Gill 2000; Bluestein et al. 2003; Lee and Wurman 2005). The vortex and its environment are allowed to translate. Vertical shear is not accounted for in the model at this time, but will be implemented in the future. In the meantime, however, because of the small elevation angles and analysis subvolumes used in our experiments, there is little aliasing of vertical shear into the horizontal. A total of 15 parameters characterize the wind field in our low-order model. These parameters are considered constant over a single 4D retrieval domain. Thus, the low-order model will be violated in cases where the observed wind field rapidly evolves in time. Although our current low-order model is independent of height, the ARPS model fields used in the later tests do vary with height, and so provide a stringent test of the current model formulation.

The Cartesian components of the linear flow fields (broad-scale flow) are given by

$$\begin{aligned} V_x &= a + b(y - v_t t) + c(x - u_t t) \quad \text{and} \\ V_y &= d + e(x - u_t t) + f(y - v_t t), \end{aligned} \quad (1)$$

where  $a$  and  $d$  are constant flow components,  $b$  and  $e$  are shear parameters,  $c$  and  $f$  are divergence parameters,  $u_t$  and  $v_t$  are the translational velocity components of the broad-scale fields, and  $t$  is time. It can be noted that (1) implicitly makes provision for a broad-scale vortex since the Cartesian representation of a solid-body vortex is  $u = -\Omega y$ ,  $v = \Omega x$ , where  $\Omega$  is the (constant) vortex angular

velocity. This broadscale vortex description is independent of the small-scale vortex model to be described next.

In a local cylindrical coordinate system centered on and translating with the modified combined Rankine vortex, the azimuthal velocity field  $v_\theta$  and radial velocity field  $v_r$  are given by

$$v_\theta = \begin{cases} \frac{r}{R} V_T, & r < R, \\ \frac{R^\alpha}{r^\alpha} V_T, & r \geq R, \end{cases} \quad \text{and } v_r = \begin{cases} \frac{r}{R} V_R, & r < R, \\ \frac{R^\beta}{r^\beta} V_R, & r \geq R, \end{cases} \quad (2)$$

where

$$r = \sqrt{(x - x_0 - u_t t)^2 + (y - y_0 - v_t t)^2}, \quad (3)$$

is the distance of a given  $(x, y)$  coordinate from the center of the vortex at time  $t$ . The vortex is described by seven parameters: the initial vortex-center location  $(x_0, y_0)$ , the radius of maximum wind  $R$ , the maximum tangential velocity  $V_T$ , the maximum radial velocity  $V_R$ , and the radial decay rates  $\alpha$  and  $\beta$  of the tangential and radial wind components. The translational velocity components  $u_t$  and  $v_t$  are the same as in the broadscale model in (1). The model parameters are listed in Table 1.

To facilitate calculation of the radial (with respect to a radar) component of the model wind fields, the Cartesian components of the model wind fields are first

obtained and then the radial component is extracted. Toward that end, the velocity  $\mathbf{V}$  of the MCRV can be expressed in vortex-centered cylindrical coordinates (not radar coordinates) as the sum of its radial and tangential components,  $\mathbf{V} = v_r \hat{\mathbf{r}} + v_\theta \hat{\boldsymbol{\theta}}$ , where  $\hat{\mathbf{r}}$  and  $\hat{\boldsymbol{\theta}}$  are the unit vectors in the radial and azimuthal directions in the vortex cylindrical coordinate system, respectively. Figure 1 depicts the relationship between the Cartesian and vortex coordinate systems. The Cartesian components of  $\mathbf{V}$  are computed as

$$u = \hat{\mathbf{i}} \cdot \mathbf{V} = v_r \cos\theta - v_\theta \sin\theta \quad \text{and} \quad v = \hat{\mathbf{j}} \cdot \mathbf{V} = v_r \sin\theta + v_\theta \cos\theta. \quad (4)$$

Formulas for  $\cos\theta$  and  $\sin\theta$  at arbitrary time  $t$  follow immediately from Fig. 1:

$$\cos\theta = \frac{x - x_0 - u_t t}{r} \quad \text{and} \quad \sin\theta = \frac{y - y_0 - v_t t}{r}.$$

Substituting these into (4) yields

$$u = \frac{x - x_0 - u_t t}{r} v_r - \frac{y - y_0 - v_t t}{r} v_\theta \quad \text{and} \\ v = \frac{y - y_0 - v_t t}{r} v_r + \frac{x - x_0 - u_t t}{r} v_\theta.$$

Substituting for  $v_r$  and  $v_\theta$  from (2) and adding the linear flow fields in (1) produce the Cartesian representation of the full model wind field:

$$u = \begin{cases} a + b(y - v_t t) + c(x - u_t t) + \frac{V_R}{R}(x - x_0 - u_t t) - \frac{V_T}{R}(y - y_0 - v_t t), & r < R, \\ a + b(y - v_t t) + c(x - u_t t) + \frac{R^\beta V_R(x - x_0 - u_t t)}{r^{\beta+1}} - \frac{R^\alpha V_T(y - y_0 - v_t t)}{r^{\alpha+1}}, & r \geq R, \end{cases}$$

and

$$v = \begin{cases} d + e(x - u_t t) + f(y - v_t t) + \frac{V_R}{R}(y - y_0 - v_t t) + \frac{V_T}{R}(x - x_0 - u_t t), & r < R, \\ d + e(x - u_t t) + f(y - v_t t) + \frac{R^\beta V_R(y - y_0 - v_t t)}{r^{\beta+1}} + \frac{R^\alpha V_T(x - x_0 - u_t t)}{r^{\alpha+1}}, & r \geq R. \end{cases}$$

Finally, solving for the radial component of the total velocity yields the model Doppler radar velocity  $V_r^{\text{mod}}$ :

$$V_r^{\text{mod}} = \cos\phi_n \sin\theta_n \left[ a + b(y - v_t t) + c(x - u_t t) + \frac{V_R}{R}(x - x_0 - u_t t) - \frac{V_T}{R}(y - y_0 - v_t t) \right] \\ + \cos\phi_n \cos\theta_n \left[ d + e(x - u_t t) + f(y - v_t t) + \frac{V_R}{R}(y - y_0 - v_t t) + \frac{V_T}{R}(x - x_0 - u_t t) \right], \quad r < R, \\ = \cos\phi_n \sin\theta_n \left[ a + b(y - v_t t) + c(x - u_t t) + \frac{R^\beta V_R(x - x_0 - u_t t)}{r^{\beta+1}} - \frac{R^\alpha V_T(y - y_0 - v_t t)}{r^{\alpha+1}} \right] \\ + \cos\phi_n \cos\theta_n \left[ d + e(x - u_t t) + f(y - v_t t) + \frac{R^\beta V_R(y - y_0 - v_t t)}{r^{\beta+1}} + \frac{R^\alpha V_T(x - x_0 - u_t t)}{r^{\alpha+1}} \right], \quad r \geq R. \quad (5)$$

TABLE 1. True values of low-order model parameters used in analytical retrievals and the retrieved values from a set of eight retrievals (EXP1) and one single retrieval (EXP2).

Parameter	Description	True value	EXP1 mean retrieved value	EXP1 std dev	EXP2 retrieved value
$a$ ( $\text{m s}^{-1}$ )	Uniform flow	10	9.4	0.7	11.6
$d$ ( $\text{m s}^{-1}$ )	Uniform flow	10	9.4	0.4	11.2
$b$ ( $\text{s}^{-1}$ )	Shear amplitude	0.002	0.0023	0.0004	0.0012
$e$ ( $\text{s}^{-1}$ )	Shear amplitude	0.002	0.0021	0.0004	0.0024
$c$ ( $\text{s}^{-1}$ )	Divergence amplitude	0.0015	0.0019	0.0002	0.0010
$f$ ( $\text{s}^{-1}$ )	Divergence amplitude	0.002	0.0024	0.0004	0.0014
$R$ (m)	Radius of max wind	200	202	11	309
$V_R$ ( $\text{m s}^{-1}$ )	Max radial wind	-10	-9.9	1.0	-9.4
$V_T$ ( $\text{m s}^{-1}$ )	Max tangential wind	50	48.3	1.4	38.6
$x_0$ (m)	Vortex center	5000	4997	9	5003
$y_0$ (m)	Vortex center	5000	4998	10	4997
$u_t$ ( $\text{m s}^{-1}$ )	Translational velocity	-10	-9.9	1.8	-10.1
$v_t$ ( $\text{m s}^{-1}$ )	Translational velocity	-10	-10.0	1.6	-9.9
$\alpha$	Vortex wind decay	0.7	0.687	0.056	0.75
$\beta$	Vortex wind decay	0.4	0.374	0.135	0.78

where  $\theta_n$  and  $\phi_n$  are the azimuth and elevation angles, respectively, of the  $n$ th radar ( $\theta_n$  is measured clockwise from the north). In some of the analytical experiments presented below, a cylindrical approximation to the true spherical geometry was used. This approximation is justified by the small elevation angle ( $0.5^\circ$ ) used in these experiments.

### 3. Cost function computation and minimization

The (squared) discrepancies between the observed and model-predicted radial wind fields are summed over the spatial-temporal domains of  $N$  radars, each scanning in range  $r_n$ , azimuth  $\theta$ , and elevation angle  $\phi$ . By taking the translation of the broadscale flow and vortex into account, discrepancy calculations for the radial wind model can be performed at the same locations and times as the observations.

Since radar resolution volumes increase in size with distance from the radar, Doppler velocity observations become representative of winds over a larger region as range increases. A range-weighting factor,  $r_n/r_{\text{mean}}$ , is introduced to account for this. In reality, radar resolution volumes increase as the square of range (spherical coordinate probe volumes), but in our experiments with analytical and numerically simulated data, resolution volumes are considered to be flat (cylindrical coordinate probe areas). However, it has been verified in other of our experiments (not shown) that the results are very similar regardless of which of these weighting functions is used. In our experiments with real data, the proper range-weighting factor,  $r_n^2/r_{\text{mean}}^2$ , is used.

The cost function  $J$  accounting for the discrepancies between the observed and model-predicted radial wind fields is

$$J \equiv \sum_{n=1}^N \sum_{m=1}^M \sum_{\phi} \sum_{\theta} \sum_{r_n} \left[ \frac{r_n}{r_{\text{mean}}} (V_r^{\text{obs}} - V_r^{\text{mod}})^2 \right], \quad (6)$$

where  $M$  is the total number of full volume scans (temporal sum) and  $r_n$  is the radial distance of a point from the  $n$ th radar (the range-weighting factor is appropriately modified in experiments with real data as described above). Here  $J$  provides a useful way to quantitatively compare the quality of retrievals for different experiments, and, when appropriately normalized, can be used to calculate the mean model error per radar grid point.

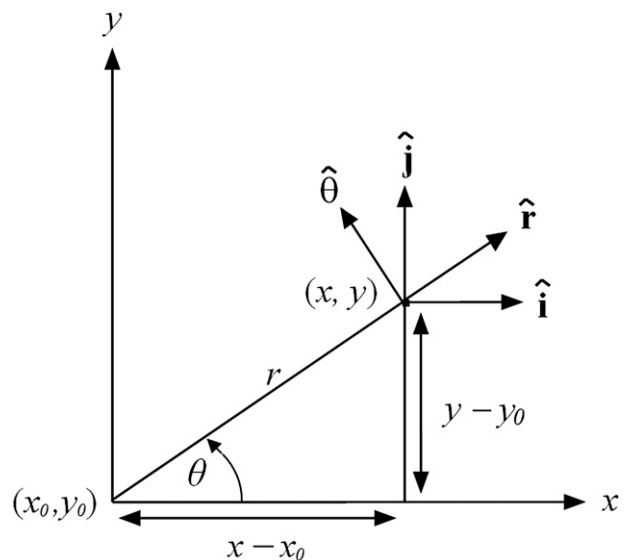


FIG. 1. Cartesian and cylindrical (vortex) coordinate systems defining model broadscale and vortex flows, respectively, at  $t = 0$ . The vortex is initially located at  $x_0, y_0$ .

The cost function  $J$  is minimized to retrieve the set of parameter values producing the least squares error in the model wind (best fit between model and observed winds). In view of (6) and the location of the model parameters in (5), our minimization problem is highly nonlinear. Conjugate gradient minimization methods have proven useful for such problems. The minimization algorithm used in this technique is the Polak–Ribiere (1969) method, a robust and efficient variant of the Fletcher and Reeves (1964) algorithm. In both methods, the search direction is reset to that of steepest descent (with all previous direction and gradient information being discarded) every  $p$  iterations, where  $p$  is the number of model parameters.

In the analytical and ARPS experiments presented herein, the minimization algorithm was modified such that certain key model parameters are reset to their initial values if they exceed specified bounds. In particular,  $x_0$ ,  $y_0$  are reset whenever the provisional vortex center comes within a distance  $R$  (radius of maximum wind) of the edge of the analysis domain (the reason is discussed in section 5). In addition,  $R$  is constrained to be larger than 10 m since vortices smaller than this are unlikely to be resolved by even a CASA-like radar network, and since negative values of  $R$  are physically impossible but could be obtained computationally.

As with other minimization techniques, multiple minima in  $J$  can prevent the global minimum from being reached. Local minima in the current problem can result from the intrinsic nonlinearity of the problem, as well as from areas of missing data and departures of the observed wind field from the model.

The threat of local minima increases as the surface of the cost function becomes more elliptical. To reduce the ellipticity of  $J$  and thus increase the convergence rate of the minimization algorithm, the first-guess vector is scaled such that the gradients of  $J$  with respect to each of the parameters become closer in magnitude (as in Wang et al. 1997). To accomplish this, the scaling factors are set equal to physically realistic values of each of the parameters. Experiments have shown the technique to be relatively insensitive to the selection of scaling factors for physically reasonable ranges of these factors.

#### 4. Analytically and numerically simulated data

##### a. Simulating the observations

The low-order technique is tested with two kinds of idealized wind fields: (i) analytically generated vortices with surrounding broadscale flow, and (ii) ARPS-simulated wind observations of a tornado-like vortex and its near environment. Analytical data were calculated

from the low-order model equations, and thus represent an overly optimistic (identical twin) framework. However, significant random errors (described below) were added to the analytical radial wind data in order to partially mitigate this problem. Both the idealized nature of the input wind field and the ability to specify the true wind parameter values facilitated testing of the algorithm code and identification of potential problems inherent to the technique. In contrast, the ARPS-simulated tornado is not constrained by the low-order model and therefore poses a greater challenge to the technique. On the other hand, there is some subjectivity in determining the “true” values of model parameters for the ARPS vortices; this is not a major concern for reasons discussed later. Data in the ARPS experiments are trilinearly interpolated from the ARPS grid to the radar domain. Since the latter domain is generally coarser than the ARPS domain, the radial wind field sampled by the algorithm loses some of the finer features in the ARPS wind field, particularly at larger ranges from the radar.

To simulate weighted averaging of actual radar moment data within a resolution volume, simple range- and beam-weighting functions (no power weighting) are applied to a distribution of hypothetical scatterers within each resolution volume in both the analytical and ARPS experiments. The range weight at a given point within the resolution volume is defined by a trapezoid function with a value of unity between 20 and 80 m along the beam and linearly decreasing to zero at the edges of the resolution volume (range resolution = 100 m). This weighting function is similar to one used to emulate a WSR-88D range pattern (Wood et al. 2004). The azimuthal weight is given by

$$W_{az} = \exp \left[ -8 \ln 2 \left( \frac{\theta - \theta_0}{\theta_B} \right)^2 \right], \quad (7)$$

where  $\theta_0$  is the azimuth of the center of the beam and  $\theta_B$  is the half-power beamwidth, which is set to  $2^\circ$  in most of our ARPS experiments (to be consistent with the half-power beamwidth of current CASA radars) and to  $1^\circ$  in the analytical experiments (to verify the code is free of error). The scanning strategy used in our experiments is further discussed in section 4d.

##### b. Analytical data

In most of the analytical experiments, Gaussian random errors [generated using the Box and Muller (1958) method] were added to the volume-averaged observations, with the first standard deviation of the percent error distribution lying between  $-30\%$  and  $30\%$ , and the portions of the distribution beyond  $\pm 50\%$  being

truncated at  $\pm 50\%$ . These large input errors represent serious contamination of the otherwise “optimistic” test data. No error was added to  $V_r$  observations in the ARPS experiments described below because (i) the ARPS data do not have to satisfy the low-order model (indeed, significant asymmetries not accounted for in the low-order model are evident in the ARPS fields) and (ii) the ARPS data are themselves “noisy” on the grid scale. Table 1 lists the model parameter values used to generate the input wind field in the retrieval experiments described in section 5.

### c. ARPS simulation

The numerically simulated supercell/tornado data used to test the algorithm were generated in a very high-resolution run of the ARPS model [case considered in Xue et al. (2007)]. The model thunderstorm was initiated by a thermal bubble placed in a homogeneous environment defined by a sounding proximate to the 20 May 1977 Del City, Oklahoma, supercell storm. Computations were performed over a  $48 \text{ km} \times 48 \text{ km}$  domain with 50-m horizontal grid spacing and a stretched vertical grid spacing increasing from 20 m at the surface to about 80 m at 1 km AGL to 380 m at 16 km AGL. The simulation used in this study was performed with a 25-m horizontal grid spacing over a 30-min period centered on the time at which the 50-m grid tornado was most intense (the initial condition for the 25-m run consists of data interpolated from the 50-m grid simulation). Time splitting was used to integrate acoustic waves on a finer temporal scale than used for the other processes. The integration was performed with large and small time steps of 0.125 and 0.04 s, respectively. Because of the large storage requirement (over 100 MB) for each volume of data over the subdomain used in our retrieval experiments, output data were only made available to the algorithm at 10-s intervals. The data used in our retrieval experiments begin  $\sim 13\,200$  s into the simulation (600 s after the initialization of the 25-m simulation). All references to time are relative to this 13 200-s simulation time. The integration proceeded in a translating reference frame chosen to maintain the parent storm near the domain center throughout the duration of the simulation. Subgrid-scale turbulence was assumed to be isotropic, and the 1.5-order TKE turbulent mixing formulation by Moeng and Wyngaard (1989) was used. The Kessler-type warm rain microphysics was used.

Figure 2 shows the reflectivity field (based on rain-water mixing ratio) at the initial time ( $t = 290$  s after the beginning of our dataset) of some of our retrieval experiments. The tornado center appears to be collocated with the minimum in the near-surface pressure field at  $x = 3925$  m,  $y = 4425$  m. This places the tornado along

the leading edge of the hook echo signature, as is commonly observed. The tornado vortex is surrounded by a reflectivity ring. A close-up view of the wind vectors in the tornado-like vortex (hereafter referred to as a “tornado”) and the broader, weaker circulation in which it is embedded is presented in Fig. 3. The degree to which the simulated tornado resembles actual tornadoes at fine scales is not of major concern here since any differences would be barely discernable in the (relatively coarse) emulated radial velocity data. Instead, the ARPS dataset is used to test the retrieval method for a complex asymmetric flow with vortices that have a similar scale to observed tornadoes and that in many cases are near the limits of observation resolution.

### d. Scanning strategy

The radar-vortex geometrical configuration used in the majority of our experiments is depicted in Fig. 4. Two radars are positioned to give a cross-beam angle of  $\sim 90^\circ$  at the location of the vortex. In experiments with the ARPS simulation, the tornado is located roughly 28 km from both radars, which are separated by 40 km (representative of a CASA radar network). In contrast, in the analytical experiments, a radar-vortex distance of only  $\sim 7$  km was used. This admittedly optimistic configuration was adopted to facilitate verification of the code and identification of any obvious defects in the basic formulation. In the ARPS experiments, wind data are simultaneously valid over the spatial domain at each model time step and so each individual radar sector scan is assumed instantaneous on one elevation angle. In the analytical experiments, sector scans over a single elevation angle take 3.6 s. Unless stated otherwise, a return period of 30 s between three consecutive radar scans is used in the analytical experiments, giving a temporal domain of 70.8 s. A return period of 60 s between two consecutive radar scans is used in the majority of the ARPS experiments. Such short return periods are possible with CASA radar systems because they are designed to dynamically adapt their scanning strategy to the type(s) of weather present in the network (e.g., sector scanning an intense low-level circulation). The radars sample at 100-m range intervals, every  $0.5^\circ$  or  $1.0^\circ$  in azimuth, and over a single elevation angle of  $0.5^\circ$ . The beamwidth was set to  $1.0^\circ$  in the analytical experiments and in one set of ARPS experiments; a beamwidth of  $2.0^\circ$  was used in the remaining ARPS experiments.

### e. First-guess parameter values

In the analytical experiments, first-guess (FG) errors were typically set to  $+50\%$  of the true parameter values (see Table 1). The exception was the FG vortex-center error, which was typically set to 0.5–1.84 km.

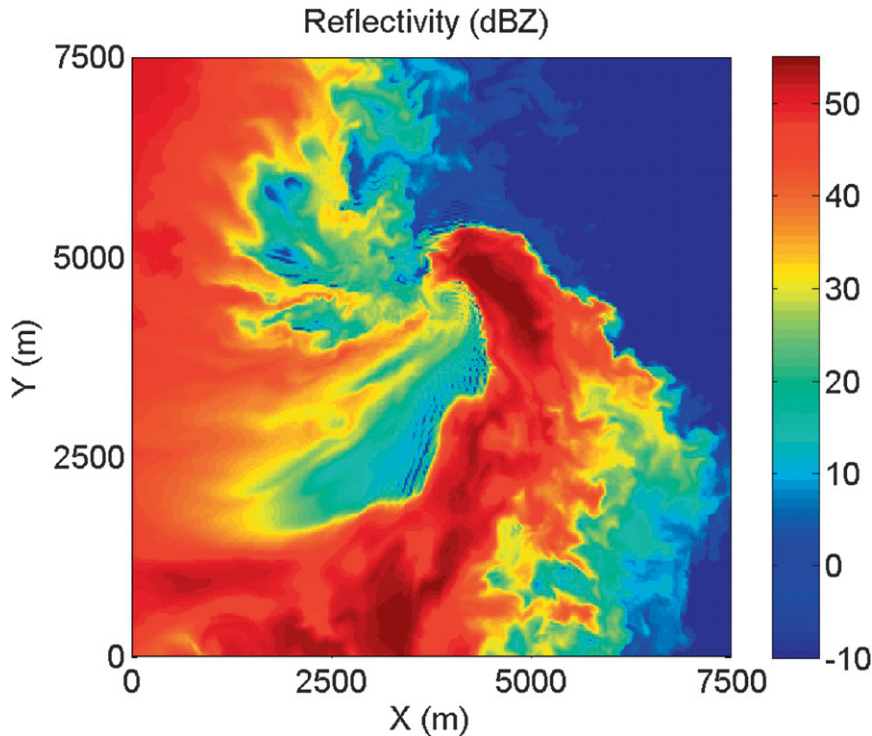


FIG. 2. ARPS reflectivity field (dBZ) at  $z = 108$  m AGL and  $t = 290$  s.

In the experiments with ARPS data, the first guess for most parameters was set to zero. First guesses of 100 m, 0.7, and 0.7 were used for  $R$ ,  $\alpha$ , and  $\beta$ , respectively. A 500-m grid of nine FG vortex centers (each corresponding to a separate retrieval) was centered on the estimated ARPS tornado center, which was assumed to be collocated with the minimum in the horizontal pressure field near the height of the observations.

The experiments with real radar observations used the same first guesses as in the ARPS experiments, except that the location of the FG vortex-center grid was objectively determined (details in section 7).

## 5. Analytical test results

### a. Sensitivity to first-guess vortex center

To assess the impact of error in the first guess for the vortex center, eight retrievals were performed with analytical data using FG vortex-center values with errors of 1.4 or 1.84 km (+50% FG errors were used for the remaining parameters; see Table 1 for the true parameter values). It is important to note that in our analytical experiments, only observations taken within a circular 2-km radius domain centered on the FG vortex center are used. All four retrievals with 1.4-km error

converged to a solution very close to truth. However, in the retrievals with the 1.84-km error in FG vortex center, the provisional vortex center exited the analysis domain during the minimization procedure. The failure of the algorithm to converge to the desired solution was likely due in part to the relatively low values of  $J$  when the provisional vortex center is near the edge of the analysis domain. The tendency for  $J$  to decrease near the edge of the analysis domain in these experiments is due to the fact that the misfit between the observed wind field and an erroneously positioned model vortex is smaller when more of the model vortex wind field is outside the analysis domain.

An example of the impact of the data boundary is depicted in the plot of  $J(x_0, y_0)$  for the case where the true vortex location is (5000 m, 5000 m), the FG vortex location is (3700 m, 3700 m), and the remaining parameters are set to their FG values (Fig. 5). During this particular retrieval, the provisional vortex center migrated toward the middle of the lower edge of the plot, which might be expected given the topography of  $J$ . Failure to retrieve the vortex center prevented the retrieval of the remaining vortex parameters.

The potential for a provisional vortex center to diverge from the desired solution (and possibly leave the analysis domain or converge to a spurious minimum)

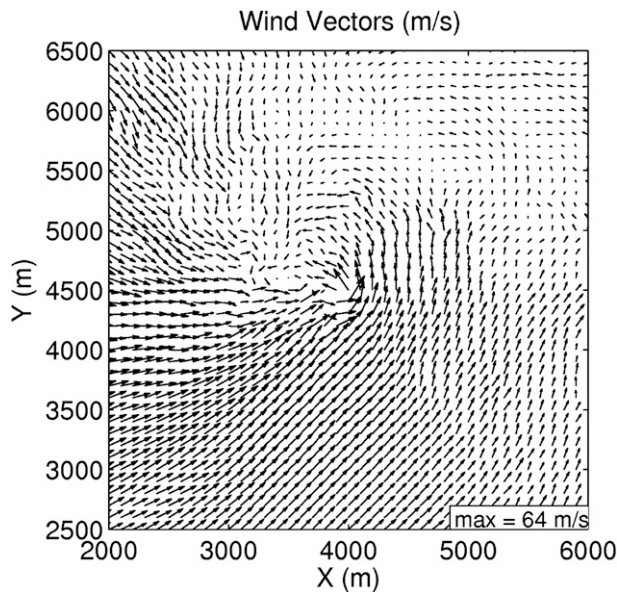


FIG. 3. Horizontal wind field in and around ARPS-simulated tornado at  $z = 108$  m and  $t = 290$  s. Only vectors at every fourth grid point are displayed.

increases with the error in the FG vortex center. In practice, multiple minima in  $J$  may also occur when a vortex is near a large area of missing data, or when the low-order model is violated. Dual-Doppler analyses (Wurman et al. 2007a,b) and numerical simulations (Wicker and Wilhelmson 1995; Xue et al. 2007) of tornadic storms indicate that the near-tornado wind field can be highly complex in nature, often consisting of other, nontornadic vortices. Multiple first guesses for the vortex center should therefore be used in order to maximize the probability of successfully identifying all vortices present. This approach is used in the GBVTD-simplex center finding algorithm (Lee and Marks 2000). In our technique, these first guesses could be supplied by existing algorithms that use shear thresholds to detect strong circulations (e.g., the TDA, MDA, and LLSD). The FG values of the remaining low-order model parameters are not varied since the success of the algorithm is much less sensitive to error in these parameters.

#### b. Sensitivity to observational error

A set of eight experiments (EXP1) was performed in which different realizations of Gaussian random errors were added to the emulated radial wind observations. The FG vortex-center error was set to 1.4 km, and +50% error was added to the remaining model parameters. Table 1 lists the mean and standard deviation of the set of retrieved values for each parameter. The agreement between the retrieved and true parameter

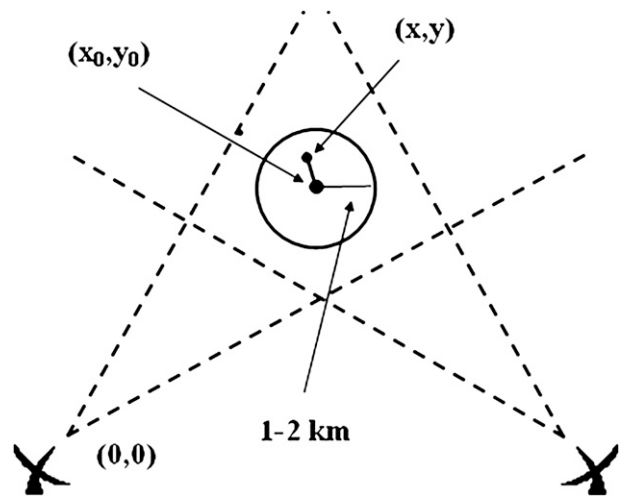


FIG. 4. Radar-vortex geometry and analysis domain.

values is generally very good, indicating that the technique is not unduly sensitive to random observational error.

#### c. Vortex parameter nonuniqueness

To assess the capability of the algorithm in a less optimum radar-vortex geometrical configuration, a set of four retrieval experiments (EXP2) was performed using a beamwidth of  $2.0^\circ$  (with  $1.0^\circ$  oversampling) and a radar-vortex distance of  $\sim 28$  km as in the ARPS experiments (to be described later). The FG error in each retrieval was 500 m for the vortex center and +50% for the remaining model parameters. A perfect observation set was used in order to isolate the effects of coarser resolution. Tests redone with observational error produced similar results (not shown) to those described

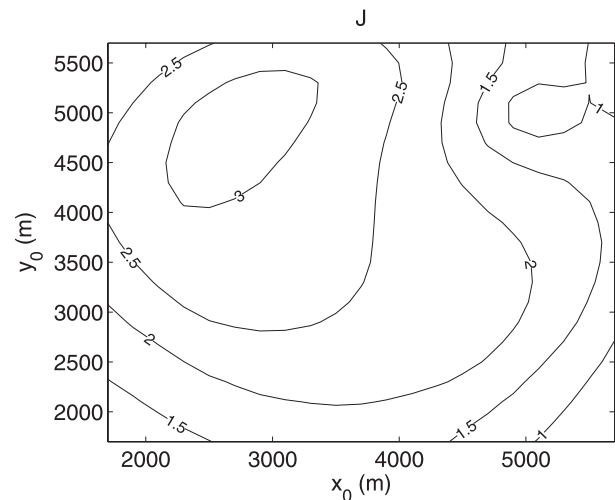


FIG. 5. Plot of  $J(x_0, y_0)$  ( $10^6 \text{ m}^2 \text{ s}^{-2}$ ) with remaining model parameters set equal to their first guesses.

below. The true and mean retrieved parameter values are listed in Table 1. Significant errors occurred in  $R$ ,  $V_T$ , and  $\beta$  (up to 61%, 26%, and 97%, respectively). Cross-sectional plots of  $J$  with respect to these parameters (not shown) for the total retrieved parameter set contain highly eccentric elliptical regions near the true solution. These elliptical regions correspond to long flat valleys in the higher-dimensional space. The elliptical regions result from the mathematical nature of the low-order model. The finite observational resolution combined with this ellipticity of  $J$  produces local minima that can prevent the desired solution from being obtained. The most significant effect of the nonuniqueness was to overestimate  $R$  and underestimate  $V_T$  or vice versa. This has important implications for the development of suitable tornado detection criteria and characterization methods for this technique (section 6d). On the other hand, in cases where the inner structure of the tornado is well resolved, vortex parameter nonuniqueness does not occur.

#### d. Broadscale translation parameter nonuniqueness

Experiments with analytically generated data were performed to see if two additional parameters (i.e., not 1 of the 15 parameters listed in Table 1) accounting for broadscale shear and divergence translation components ( $u_b$ ,  $v_b$ ) could be retrieved separately from the vortex translation components. Figure 6 shows a plot of  $J(u_b, v_b)$  for the case where the remaining model parameters are set to their true values and no error is added to the radial wind observations. The global minimum in  $J$ , corresponding to the correct solution  $(u_b, v_b) = (10, 10) \text{ m s}^{-1}$ , is embedded within a highly eccentric elliptical region of  $J(u_b, v_b)$ .

The nonuniqueness in the broadscale translation parameters ( $u_b$ ,  $v_b$ ) can be explained by reformulating the low-order model in terms of  $(u_b, v_b)$  as  $cu_b + bv_b = M$  and  $eu_b + fv_b = N$ , where  $M$  and  $N$  contain the remaining variables in the radial wind equations. From linear algebra, we know there could be multiple solutions for  $(u_b, v_b)$  if the determinant of this system vanishes: that is, if  $cf - be = 0$ . Similarly, if the determinant is very small, there are many values of  $(u_b, v_b)$  that approximate the true solution (the problem is ill posed), resulting in a  $J(u_b, v_b)$  that is nearly flat close to the true solution. In initial experiments with  $(u_b, v_b)$ , the selected values of  $b$ ,  $c$ ,  $e$ , and  $f$  resulted in a very small determinant. Plots of  $J(u_b, v_b)$  (not shown) for sets of parameter values resulting in larger determinants were consequently less elliptical; however, significant errors (up to 30%) still occurred in  $u_b$  and  $v_b$ . Similar results were obtained with the ARPS-simulated wind field using estimates for the true model parameter values.

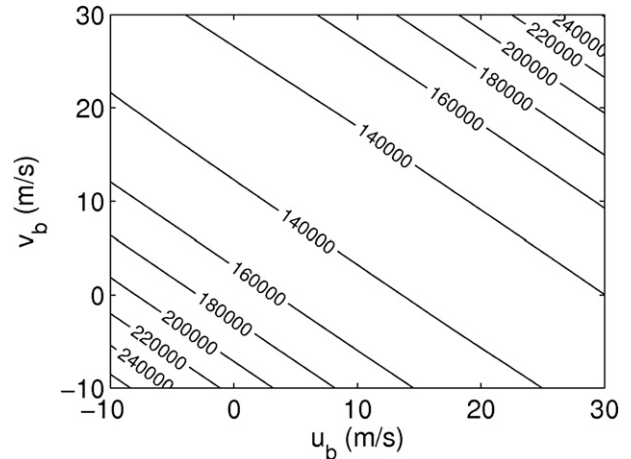


FIG. 6. The  $J(u, v)$  with perfect first guess for remaining parameters.

Since a large number of potential solutions for  $(u_b, v_b)$  may exist in practice, we will not seek these values. Fortunately, analytical and ARPS experiments with and without these variables (not shown) revealed that their omission had little negative impact on the retrieval of the remaining vortex and broadscale parameters.

## 6. ARPS test results

### a. Two-step approach in ARPS retrievals

Preliminary experiments with ARPS data demonstrated that the tornadic circulation is more reliably retrieved when a two-step retrieval procedure is adopted. In step 1, the vortex model parameters are fixed at zero (except for  $R$  since this would introduce a “division by zero” computational issue), and the broadscale parameters are retrieved. In step 2, the radial components of the wind field retrieved in step 1 are subtracted from the observed radial wind fields, and the retrieval is repeated on the residual wind field. Since the flow retrieved in step 1 (and subtracted in step 2) is much more representative of the broadscale flow than of the tornadic flow, the tornadic component of the original flow dominates the residual field to be retrieved in step 2. To make the retrieval more sensitive to the tornadic flow relative to the (presumably weaker) broadscale flow in step 2, the cost at each observation point is multiplied by the square of the observed wind:

$$J_{\text{step2}} = \sum_{n=1}^N \sum_{m=1}^M \sum_{\phi} \sum_{\theta} \sum_{r_n} \left[ (V_r^{\text{obs}})^2 \frac{r_n}{r_{\text{mean}}} (V_r^{\text{obs}} - V_r^{\text{mod}})^2 \right]. \quad (8)$$

This two-step approach was often necessary to retrieve the tornado circulation when the tornado was in close proximity to the center of a nontornadic, larger-scale circulation (low-level mesocyclone) present in the ARPS data. By virtue of their large “footprint,” large circulations may provide a better fit to the low-order model over the whole analysis domain than the smaller-scale tornado vortex. In these cases, a significant portion of the larger (and weaker) circulation is retrieved by the linear broadscale flow parameters in step 1, thereby increasing the probability that the tornadic circulation will be retrieved in step 2. Results from the two-step retrieval approach in the analytical experiments (not shown) differed little from the original one-step results shown in section 5. This is not surprising given that the emulated observations in the analytical experiments do not severely deviate from the low-order model as in the ARPS experiments.

### *b. Retrievals using ARPS tornado simulation data*

Since the sounding velocity had been subtracted from the ARPS simulation in order to keep the parent storm near the center of the computational domain, the simulated tornado moved very slowly ( $<5 \text{ m s}^{-1}$ ) relative to the two emulated radars during initial retrieval experiments. This significantly limited the capability of the technique in the cases when the tornado was poorly sampled and when only two or three volume scans from each radar were used. Presumably this is because a slow-moving tornado that is poorly sampled by the first volume scan will also be poorly sampled throughout the remaining retrieval period. To legitimately increase the rate of change of the two radar-tornado viewing angles, the emulated radars were made to translate at a velocity opposite to that which had been subtracted from the ARPS simulation. The subtracted velocity was then added back onto the ARPS wind data for kinematical consistency. The translation velocity of the observed wind field (including the tornado) relative to the radars' reference frame was thus increased to approximately  $20 \text{ m s}^{-1}$ . This framework is equivalent to one with stationary radars and a data field, which translates at the original velocity (before subtraction of storm motion). While this approach is justifiable for our present tests, it should of course be kept in mind that in real applications a poorly sampled, slowly moving tornado may well remain undetected.

The technique was applied at 30-s intervals over 14 consecutive 60-s observation periods (characteristic return period for lowest elevation angle for CASA radars) spanning a total window of 7.5 min. Each ob-

serva-tion period consisted of two instantaneous radar scans separated by 60 s. For each observation period, a retrieval was performed for each of nine FG vortex centers arranged in a grid (spacing = 500 m) centered near the true tornado center. Only observations within a circular 1.5-km radius domain centered on each FG vortex center were used. Retrieved wind fields were plotted and compared to the corresponding ARPS fields to determine how well the technique is able to recover the wind field in and near the tornado. However, quantitative comparison between retrieved and expected (based on subjective inspection of the ARPS wind field) values for the vortex parameters (other than vortex center; see below) was not attempted. There were two reasons why such an evaluation was not undertaken. First, since no mathematically rigorous definition of a tornado exists [see Lugt (1979) for an explanation of the difficulties inherent to defining vortices in general], there is no straightforward objective means of separating “tornadic” flow from “nontornadic” flow in a complex wind field. Second, the ARPS-simulated tornado does not exactly match the MCRV model and so it would be impossible to assign true values to the vortex parameters in our retrievals even if the tornadic flow could somehow be distinguished from the rest of the wind field. Retrieved values of the vortex center ( $x_0, y_0$ ) could be more confidently assessed based on the ARPS pressure field, as explained in section 6d.

During the 7.5-min period over which the series of 14 retrievals was performed, the ARPS-simulated tornado becomes increasingly intense and distinct from the surrounding flow, though a large portion of the flow surrounding the tornado is nearly as strong as the flow within the tornado vortex core during at least the first half of the test period. The ARPS wind field is considerably more complex than any of the analytical wind fields previously input to the technique, and thus provides a more stringent test of the method. In particular, multiple small-scale vortices are evident at various times in the simulation.

In each of the retrieval periods, at least one of the nine retrievals places a tornado-like vortex near the location of the simulated tornado (Table 2). The result of one such retrieval for the period 110–170 s, during which the ARPS tornado was relatively small, is shown in Fig. 7. The retrieved vortex ( $V_T = 19 \text{ m s}^{-1}$ ) is located near the simulated tornado, even though the tornado is only weakly resolved in the emulated Doppler velocity field (Fig. 8). The technique also correctly detects a vortexlike circulation west of the tornado in the 200–260-s retrieval experiment, even though this feature is not very prominent in the ARPS wind field (Fig. 9). These results indicate the technique is able to identify

TABLE 2. Number of tornado detections (out of nine retrievals) made in each of the ARPS and 8 May 2003 experiments.

Expt	No. of detections
ARPS	
170 s	1
200 s	2
230 s	5
260 s	3
290 s	3
320 s	6
350 s	6
380 s	6
410 s	7
440 s	7
470 s	6
500 s	6
Real data	
No. 1	5
No. 2	4
No. 3	4
No. 4	3
No. 5	1

intense vortices not visually evident in radial velocity data. It also highlights the desirability of using multiple first guesses to characterize all vortices within the analysis domain. However, the technique also sometimes retrieves an intense vortex where none is actually present. One of these cases is shown in Fig. 10. The location of the retrieved vortex suggests that the local minimum to which the retrieval converged may have resulted from the proximity of the data boundary [this problem was

encountered in tests with analytical data (section 5a)]. The same is true for the other three spurious vortices retrieved in these experiments (not shown), all of whose wind fields were potentially significantly truncated by the edge of the analysis domain. Fortunately, tornado-strength winds (if present) associated with these vortices existed over scales that are small relative to the observational resolution (i.e., unresolved features), thereby allowing them to be easily rejected by the detection criteria (section 6d).

In the majority of cases where the retrieved vortex is nearly collocated with the ARPS tornado, the retrieved vortex is visually similar to the ARPS tornado on scales  $\geq 100$  m (those visible in the figures herein). At later times in the simulation, the larger size of the tornado allows for much of its structure to be recovered. A representative case is shown in Fig. 11, along with an illustration of the two-step retrieval procedure. Though the relatively coarse observing resolution precludes reliable retrieval of the tornado inner core in these tests, the technique exhibits skill in retrieving the tornado wind field on radar grid scales.

*c. Experiments with sampling strategies*

In this section we describe 7 sets of 14 experiments that were performed to determine the effects of using different analysis domain sizes and radar sampling strategies (Table 3). Each set of retrievals used the same starting times and first-guess parameter values as in the experiments described in section 6b.

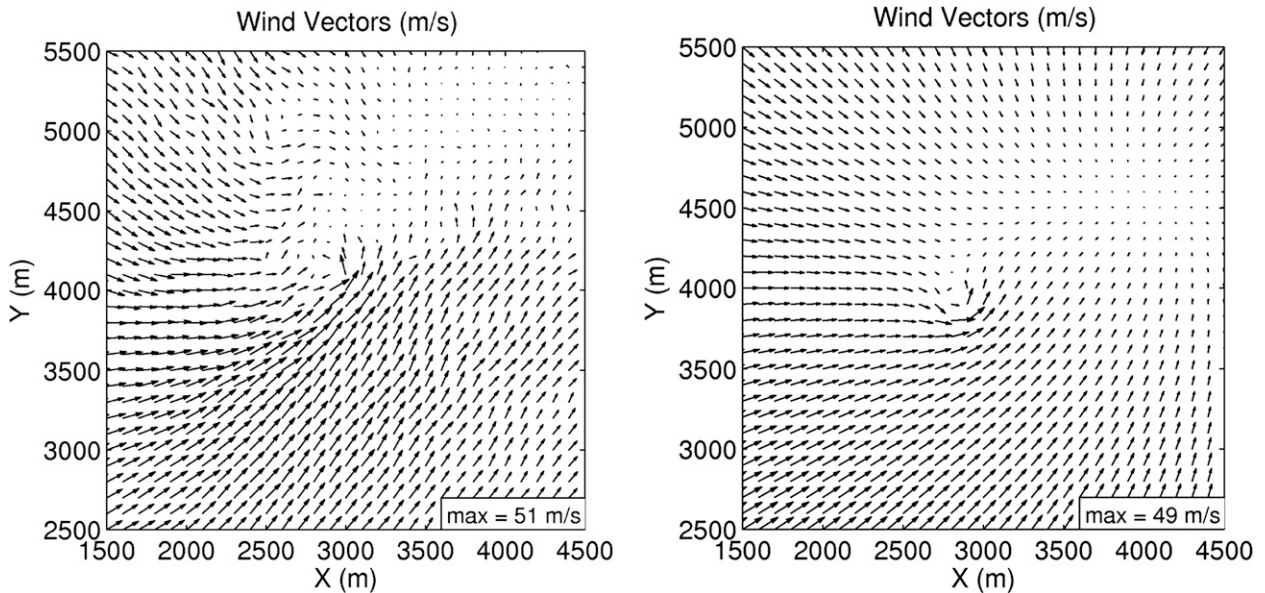


FIG. 7. (left) ARPS and (right) selected retrieved wind field at  $t = 110$  s. The plot circumscribes the analysis domain used for this retrieval. Only every fourth vector is plotted for readability.

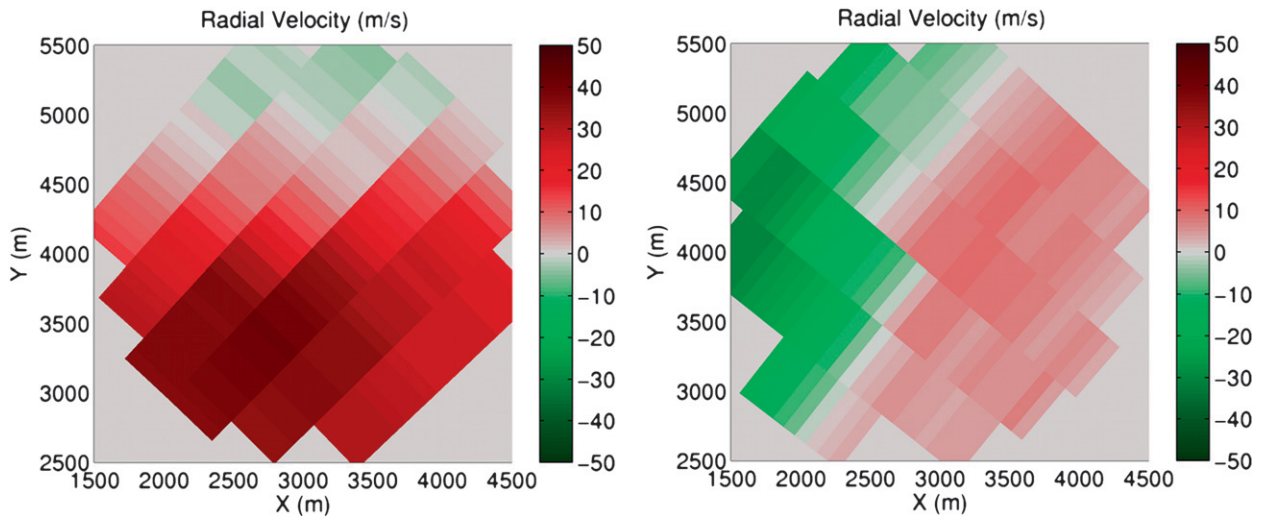


FIG. 8. Emulated radial velocity observations input to retrieval algorithm for retrieval domain shown in Fig. 7: (left)  $V_r$  from radar at  $x = -15$  km,  $y = -15$  km; (right)  $V_r$  from radar at  $x = 25$  km,  $y = -15$  km.

Increasing the analysis domain radius from 1.5 to 2 km reduced the number of successful retrievals (intense vortex retrieved close to ARPS tornado), especially at earlier times when the tornado was weaker. This degradation in the quality of retrievals is likely due to increased violation of the low-order model at larger scales. There are two major reasons for this. First, nonlinearity in the broadscale flow is more apparent on larger scales, increasing the potential for errors in the retrieved flow in step 1 of the algorithm, which can then translate into additional errors in the retrieved flow in step 2. Second, larger spatial domains are likely to contain more non-

tornadic vortexlike circulations. Of course, an analysis domain that is very small may not encompass enough of the tornado circulation. The use of a 1.5-km domain was a good compromise in these experiments.

Experiments using three rather than two scans from each radar generally led to poorer results at earlier times. This is not surprising since the ARPS tornado evolves rapidly with time while the low-order model assumes that vortex characteristics (except for location) are constant. Observations over a longer period of time are thus more likely to violate the model. Using three scans did not significantly impact the technique's performance in the

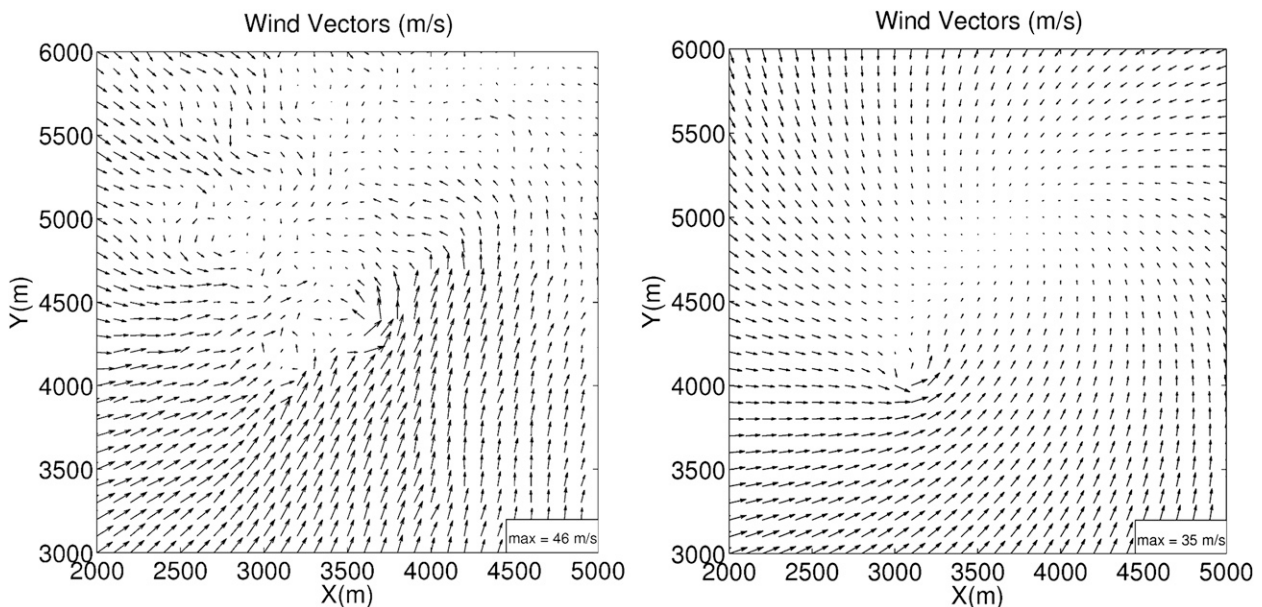


FIG. 9. As in Fig. 7, but for the period from 200 to 260 s.

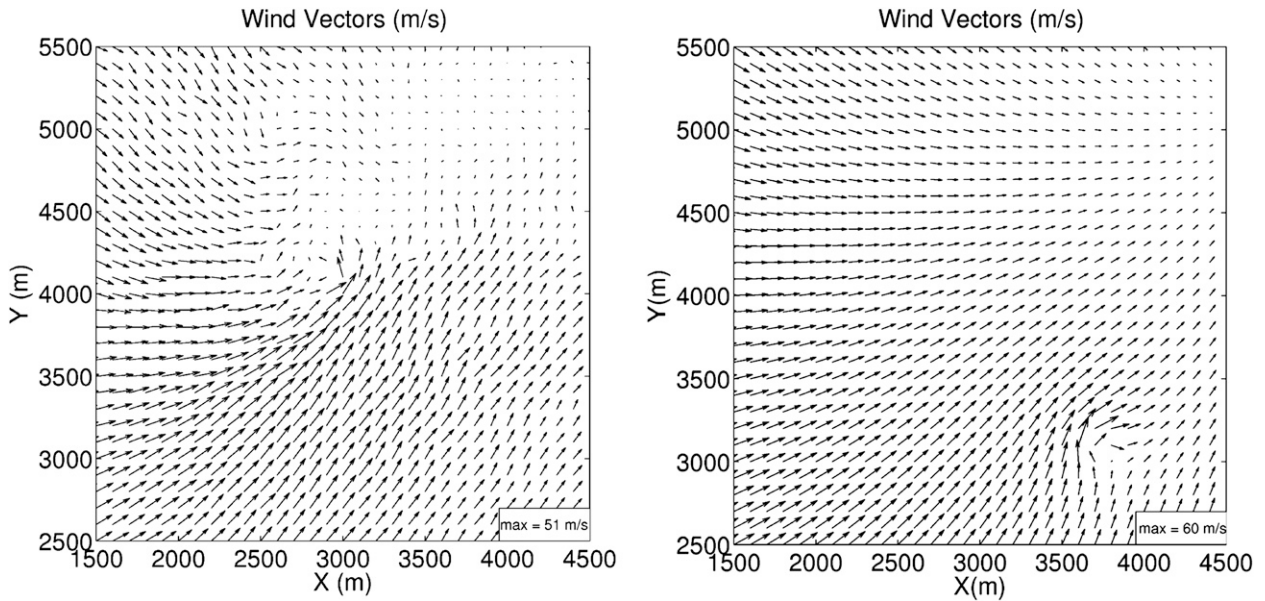


FIG. 10. As in Fig. 7, but for a different FG vortex center.

later periods when the tornado was larger, stronger, and not evolving as rapidly.

Using four scans separated by only 20 s (cf. 60 s in the previous experiment) produced slightly improved retrievals for the earlier periods, but did not produce noticeably better results when the tornado was larger and more intense. Surprisingly, decreasing the beamwidth, azimuthal sampling interval, or range resolution also did not noticeably improve the retrievals. This suggests that the greater limitation to the technique in the ARPS-data experiments was imposed by the simplicity of the low-order model (failure to capture the complexity of the ARPS-simulated tornado structure), and not by the coarseness of the observations.

Decreasing the radar cross-beam angle to  $45^\circ$  while keeping the radar-tornado distances roughly the same significantly reduced the number of retrievals (within each set of experiments with different first-guess vortex locations) in which an intense vortex was recovered very near the location of the tornado. However, at least one successful retrieval was obtained for each retrieval period except for 140–200 s, indicating that less ideal cross-beam angles do not unduly hinder the technique.

#### d. Application of detection criteria

In cases where the ARPS tornado was large relative to the radar grid scale, both the inner core and outer region of the vortex were well retrieved by the technique (e.g., Fig. 11). These results suggest that the technique yields reasonable estimates of  $R$  and  $V_T$  when the tornado is well resolved. These parameters could

therefore be useful as both vortex characteristic estimates and detection criteria in such cases. Appropriate detection criteria in cases where the tornado is well resolved could, for example, require that  $V_T$  or the angular velocity  $V_T/R$  exceed appropriate thresholds. Such thresholds will be determined based on the resulting probability of detection (POD) and false-alarm rate (FAR) values in future tests with real data.

Experiments with the ARPS tornado dataset (section 6b) demonstrated that nonuniqueness in  $R$  and  $V_T$  (due to finite radar resolution) can result in the retrieval of spurious small-scale vortices. Analytical experiments (section 5c) showed that this nonuniqueness problem can also result in underestimation of  $R$  and overestimation of  $V_T$  (or vice versa) in cases where a small vortex is correctly detected but poorly resolved. Successful detection criteria must account for these effects in cases where the retrieved vortex is not well-resolved on the radar grid scale.

In this study, we have attempted to mitigate the resolution/nonuniqueness problem by rejecting retrieved vortices whose radius of tangential  $35 \text{ m s}^{-1}$  wind,  $R_{35}$ , cannot be resolved given the observational resolution. For each retrieval in the 14 experiments in section 6b,  $R_{35}$  was calculated from Eq. (2) as

$$R_{35} = R \left( \frac{V_T}{35 \text{ m s}^{-1}} \right)^{1/\alpha}. \quad (9)$$

This formula is valid outside of the vortex core (region of solid-body rotation). A retrieved vortex was counted as a tornado detection if  $R_{35} > 100 \text{ m}$ . The 100-m threshold

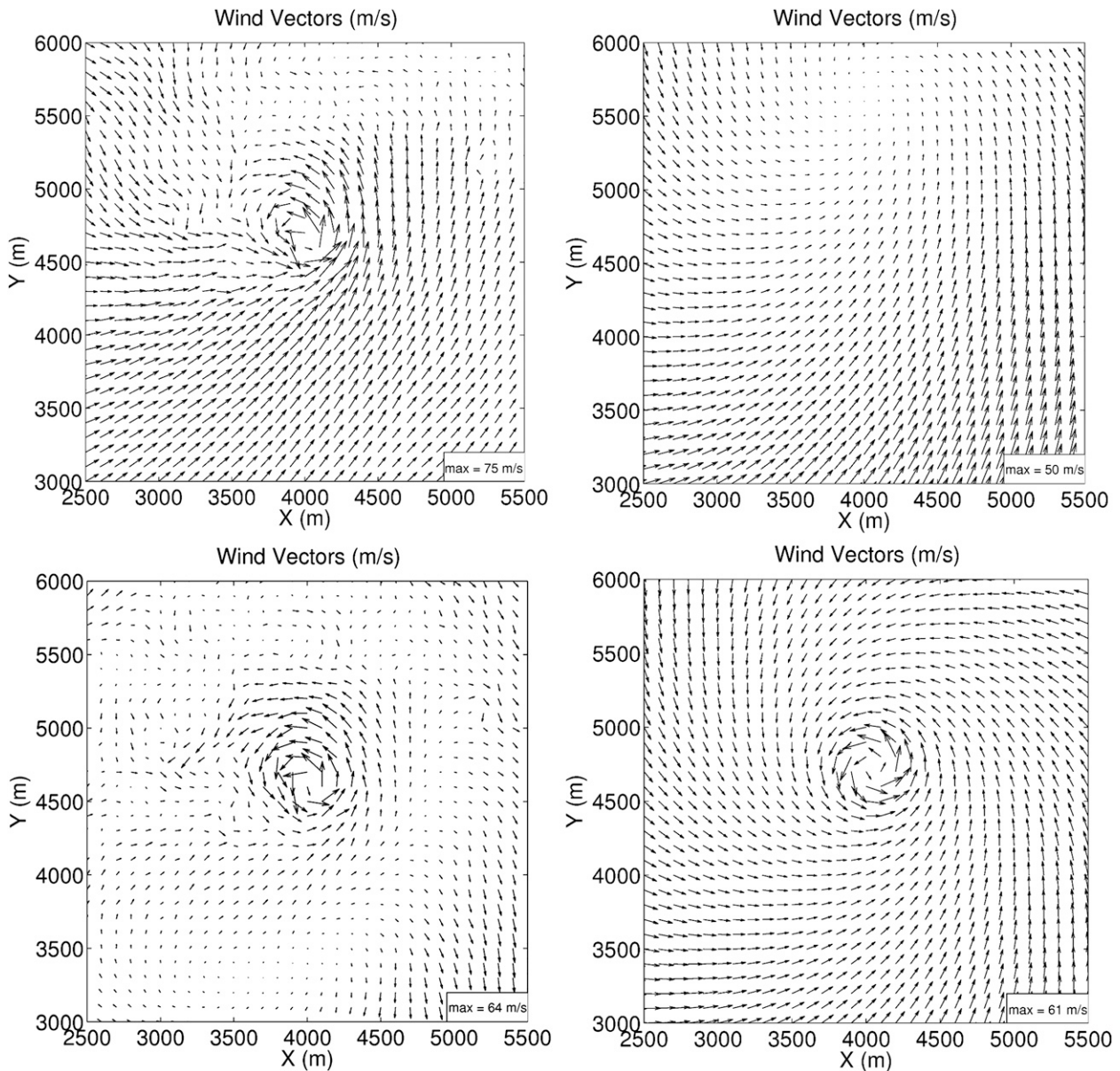


FIG. 11. Illustration of two-step retrieval procedure, valid at  $t = 410$  s: (top left) ARPS wind field, (top right) retrieved broadscale flow, (bottom left) the vector difference (top left) – (top right), and (bottom right) total retrieved flow.

is simply the smaller of the two radar sampling intervals (100 m in range and  $\sim 500$  m in azimuth). It is most appropriate in cases where the cross-beam angle is nearly  $90^\circ$ , since observations are consequently spaced every 100 m in two roughly perpendicular directions. This condition is satisfied in all of the experiments in this section.

For each of the 14 retrieval periods, retrieved vortices that did not pass this detection criterion were discarded. The mean retrieved vortex center was then calculated from the vortices that did pass the detection criterion

for each period. The mean retrieved vortex path was then compared to the ARPS tornado path as determined from the minimum in the ARPS pressure field near the height where observations were taken.

Using the  $R_{35}$  detection criterion, all of the retrieved vortices for the two earliest retrieval periods (110–170 s and 140–200 s) were rejected. Visual inspection of the 25-m ARPS wind vector plots (not shown) during these early time periods shows that the ARPS tornado would be irresolvable on our observation grid ( $R < 75$  m). Fortunately, the tornado was correctly detected in each

TABLE 3. Experiments with different sampling strategies. Each experiment set consists of 14 experiments corresponding to different start times.

Expt set	Analysis domain radius	No. of radar scans	Interval between scans	Beamwidth/sampling interval	Cross-beam angle	Gate spacing
1	2 km	2	60 s	2°/1°	90°	100 m
2	1.5 km	3	60 s	2°/1°	90°	100 m
3	1.5 km	3	20 s	2°/1°	90°	100 m
4	1.5 km	2	60 s	2°/0.5°	90°	100 m
5	1.5 km	2	60 s	1°/1°	90°	100 m
6	1.5 km	2	60 s	2°/1°	45°	100 m
7	1.5 km	2	60 s	2°/1°	90°	25 m

of the remaining 12 retrieval periods. In the majority of these cases, the tornado was detected in several of the nine retrievals, indicating the technique was not unduly sensitive to error in the first-guess vortex center (Table 2). Moreover, no spurious vortices (such as the one depicted in Fig. 10) passed the detection criterion during these times. For these 12 retrieval periods, the retrieved tornado path closely matches the ARPS pressure-estimated path (Fig. 12). The average (over the 12 retrieval periods) displacement between the two paths is only ~120 m, an encouraging result given the observational resolution in these experiments.

**7. Tests with real radar observations of a tornado**

*a. Description of dataset*

The technique was next tested using real dual-Doppler data from a high-impact event. On 8 May 2003, a supercell produced a long-lived F4 tornado in the southern portion of the Oklahoma City, Oklahoma, metropolitan area. The tornado remained within the dual-Doppler domain of the

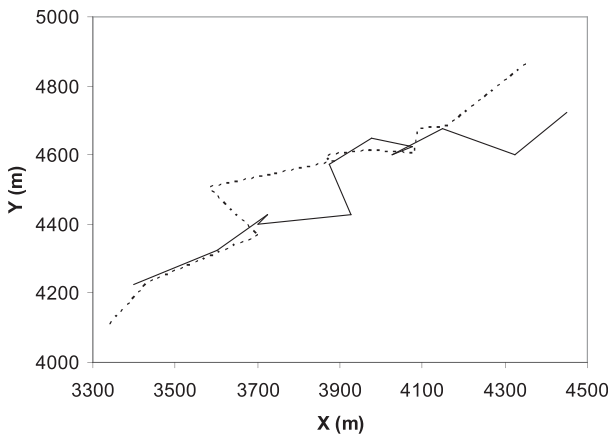


FIG. 12. ARPS-estimated tornado path (solid) and retrieved vortex path (dotted) for the period from 170 to 500 s.

TABLE 4. Selected characteristics of the KOKC and KTLX radars.

	Doppler band	Beamwidth	Azimuthal sampling	Range sampling
KTLX	S	0.95°	1.0°	250 m
KOKC	C	1.0°	1.0°	150 m

KOKC (a Terminal Doppler Weather Radar) and KTLX radars (characteristics of both radars are listed in Table 4) throughout its lifetime, during which 0.5° elevation reflectivity and radial velocity scans were performed every ~5 min by KTLX and every ~1 min by KOKC. The tornado damage path and relative locations of KOKC and KTLX are depicted in Fig. 13. A set of retrieval experiments was performed using data from five consecutive 0.5° KTLX scans along with one 0.5° KOKC scan taken within ~30–60 s of each KTLX scan. All velocity data used in the experiments were subjectively dealiased. The proximity of the tornado to both radars (11–26 km) allowed observations to be collected at an azimuthal resolution characteristic of a CASA network. However, the range resolution of these data (150 and 250 m) is coarser than that for a CASA radar (~25–100 m), and the large time interval between KTLX 0.5° scans required that retrievals be performed on single pairs of KTLX/KOKC scans rather than using multiple consecutive scans from each radar. Thus, the retrievals obtained in these experiments are presumably representative of, or somewhat poorer than, those that would have been obtained had the tornado been sampled by a network of CASA radars.

*b. Selection of analysis domains*

Using enough analysis domains to cover the entire dual-Doppler domain would, in the absence of a high performance computing cluster, require too much time

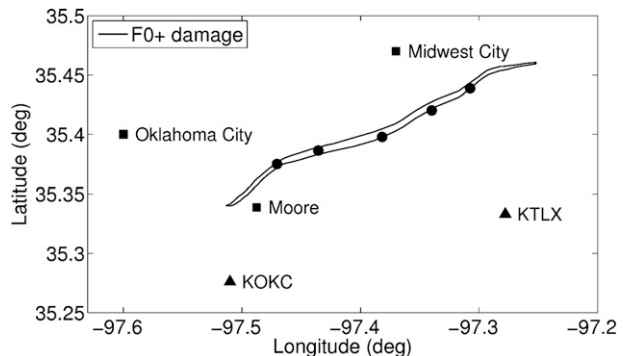


FIG. 13. Location of the tornado damage path (F0+) relative to KTLX and KOKC. The dots along the damage path indicate the tornado locations retrieved by the technique.

for the technique to be applied operationally. Therefore, the technique was modified so that retrievals are performed only in regions identified as possibly containing tornado-like vortices. The process by which these regions are selected begins by identifying all pairs of azimuthally adjacent radar gates that satisfy the following criteria: 1) azimuthal shear of radial velocity calculated between the two radar gates exceeds  $0.05 \text{ s}^{-1}$ , 2) the azimuthal distance between the two gates is less than 1 km, 3) radial velocity exceeds  $25 \text{ m s}^{-1}$  in at least one of the gates, and 4)  $<20\%$  of the velocity data is missing within both 500 and 1000 m of each of the gates. Criteria 1, 2, and 3 are intended to distinguish between tornado-like vortices and weaker or broader vortices. Criterion 4 was partly motivated by analytical experiments in which velocity data gaps produced spurious minima in  $J$  (section 5a).

For each pair of radar gates satisfying all four criteria, the centroid of the two gates is stored. Since vortices always exhibit azimuthal shear signatures in the velocity fields of both radars, all centroids that are located within 2 km of another centroid in the other radar's domain are retained. All such points are then spatially grouped into clusters (since there may be multiple proximate points associated with the same vortex) whose centroids are calculated and stored. Each centroid corresponds to the center of a region over which the retrieval technique will be applied. A grid of nine first guesses (spacing = 500 m) for the vortex center (each serving as the center of an analysis domain over which the retrieval is applied, as in the ARPS experiments) is subsequently calculated and input to the retrieval routine.

For each of the observational periods in this set of experiments, the only set of analysis domains to be objectively selected for input to the retrieval routine contained the tornado. Each set of nine retrievals required less than 1 min of computational time on a single AMD 2.6-GHz Opteron processor. It is currently unknown whether the analysis domain selection criteria are (or can be modified to be) sufficiently robust to simultaneously maintain a low number of retrieval sets and a high probability of detection over a wide range of tornado scenarios. If a large number of retrievals are needed, then parallel processing (one processor for each set of analysis domains) could be used to produce acceptable computational wall clock times.

### c. Vortex translation retrieval

The system translation parameters ( $u_i$ ,  $v_i$ ) were often poorly retrieved in preliminary experiments with real data (not shown), leading in one case to significant error in the retrieved tornado location. To address this problem, the low-order model was modified such that the

broadscale and vortex translation are retrieved independently of each other. In the experiments below, the first-guess values of the vortex translation parameters are obtained using the scalar pattern (in our case, reflectivity) advection retrieval scheme described in Gal-Chen (1982). This approach significantly improved the vortex translation retrieval in all of the experiments, thus preventing any serious errors in the vortex location estimates.

### d. Detection criteria and vortex characterization

It was demonstrated in section 5a that proximity of a vortex to a data boundary can result in spurious minima. This problem occasionally resulted in the retrieval of spurious vortices in preliminary experiments with real data (not shown). Therefore, in the experiments described below, retrievals were rejected if the magnitude of the retrieved vortex wind ( $= \sqrt{v_r^2 + v_\theta^2}$ ) exceeded  $20 \text{ m s}^{-1}$  at the edge of the analysis domain.

A retrieved vortex is identified as a tornado if  $\alpha < 1.0$  and the radius of  $30 \text{ m s}^{-1}$  tangential winds,  $R_{30}$ , exceeds 200 m. As in section 6d, the latter threshold is based on the smaller sampling interval for each radar (150 and 250 m for KOKC and KTLX, respectively). The other criterion was motivated by the occasional retrieval of spurious vortices having unrealistically large ( $>1.0$ ) values of  $\alpha$ . Such a rapid decline in  $v_\theta$  with distance from the vortex center violates the Rayleigh (1916) instability condition and therefore may not be sustainable in actual tornadoes. This hypothesis is supported by high-resolution observational studies of tornadoes (e.g., Wurman and Gill 2000; Lee and Wurman 2005; Wurman and Alexander 2005), which have found that  $\alpha$  typically varies between 0.6 and 0.8.

These detection criteria are preliminary and may well be modified or combined with additional criteria pending future tests. For example, the 200-m threshold is simply the average of the range sampling intervals for the two radars; this threshold may not be appropriate for very small cross-beam angles and so will need to be made spatially variable in future experiments. It may be advantageous to incorporate actual observational data into the detection criteria, for example, requiring at least one radial velocity or gate-to-gate shear measurement to exceed a prescribed threshold within a certain range of the retrieved vortex. It may also be desirable to create separate detection criteria for cases where the retrieved vortex is or is not well resolved in the observational data.

The mean retrieved vortex center and  $R_{30}$  are computed from the retrievals performed within each set of analysis domains. The latter parameter is intended to provide a useful estimate of the radius of damaging winds in the tornado. Mean retrieved values of  $R$  and  $V_T$

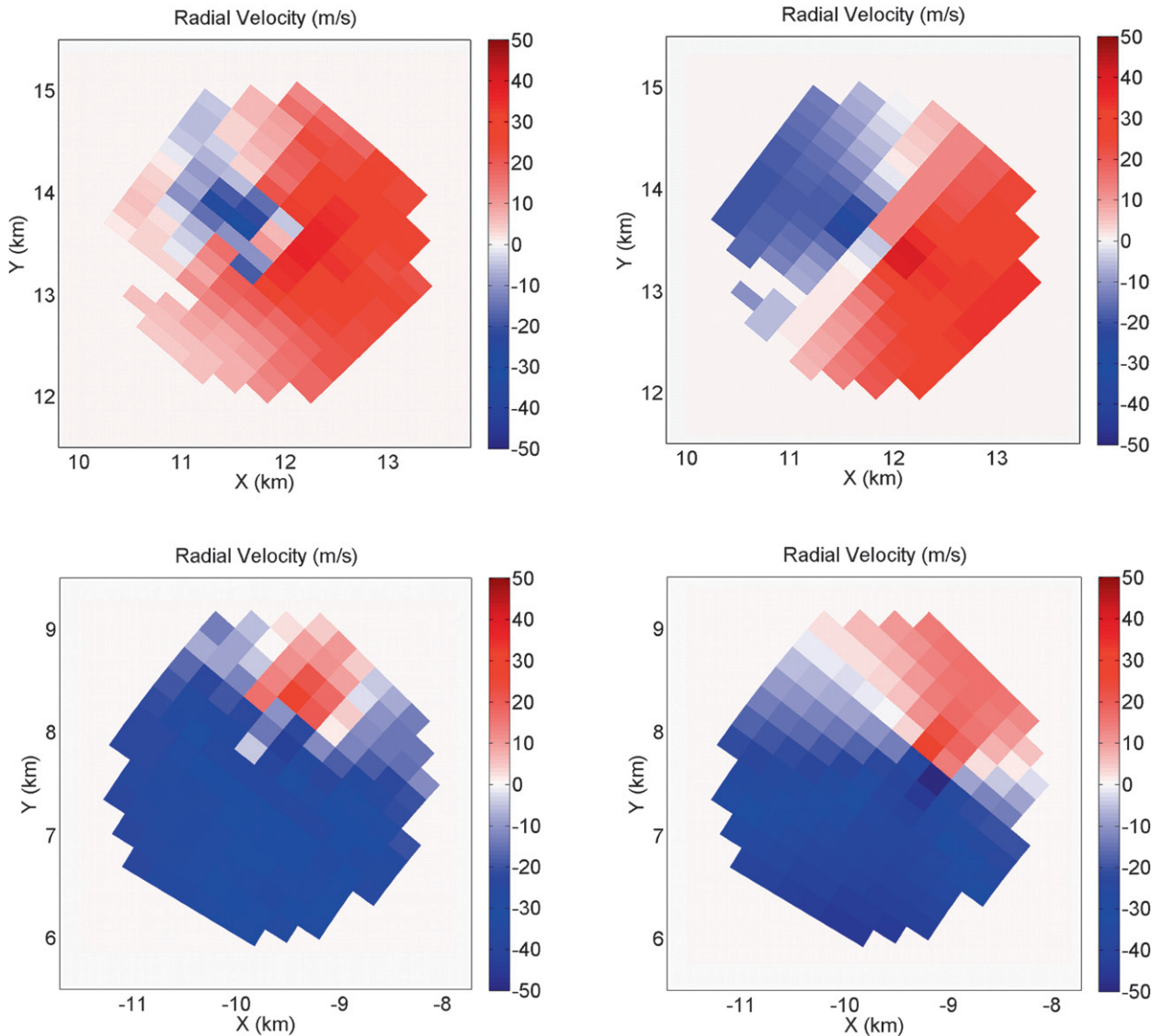


FIG. 14. (top) KTLX and (bottom) KOKC (left) observed vs (right) retrieved radial velocities.

(as well as the remaining model parameters) are also calculated, but the tornado was not sufficiently resolved in these experiments for these estimates to be reliable. Since multiple tornado-like vortices may exist within a single set of analysis domains, the technique is designed such that retrieved vortices passing the detection criteria that are located  $>1$  km from the remaining detections have their characteristics calculated separately. In the experiments presented herein, the technique correctly identifies a single tornado.

#### e. Results

The technique successfully detected the tornado during all five observational periods (Table 2), which together spanned most of the tornado's lifetime. The mean

distance between the vortex centers retrieved during each observational period (excluding the last period, during which only one detection was made) ranged from 57 to 201 m, indicating that the technique was not unduly sensitive to errors in the first-guess vortex center.

Though direct comparison of the mean retrieved vortex centers and  $R_{30}$  values to the observed damage path is hindered by several issues, most notably that the analysis domains in these experiments are  $\sim 100$ – $220$  m above the ground, the results are nevertheless encouraging. The mean retrieved vortex centers are all very nearly collocated with the observed tornado damage path (Fig. 13). The mean retrieved  $R_{30}$  for each of the experiments are (in chronological order) 248, 296, 318, 265, and 307 m, consistent with the observed maximum damage path

width of  $\sim 650$  m. The trend of  $R_{30}$  is similar to that of the damage path during the first four observational periods, while the fifth estimate is too large.

To assess how well the low-order model was able to reproduce the complexity of the input radial velocity fields, the mean retrieved wind field was compared to the observed wind field within the central analysis domain in each experiment. A representative comparison (experiment 3) is shown in Fig. 14. Naturally, the low-order model is unable to completely recover the intricate structure of the near-tornado radial wind field. However, the retrieved wind field does reasonably capture the primary structure of the tornado, at least on the scale of the observational data.

## 8. Summary and future work

A new multiple-Doppler technique for identifying and characterizing tornadoes has been presented. The method consists of fitting radial wind observations to a low-order model of a tornado-like vortex and its near environment. The technique takes advantage of the enhanced density (and therefore spatial coverage and resolution) of a CASA-like radar network. The retrieval technique has been tested against analytically generated observations, a high-resolution ARPS simulation of a tornado and surrounding wind field, and real dual-Doppler observations of a tornado. The technique exhibits skill not only in detecting tornado-like vortices within a CASA-like network, but also in retrieving the vortex location and wind field on scales greater than or equal to that of the radar grid. Characteristics of retrieved vortices, if available to forecasters in real time, could aid in the tornado warning process.

Spurious minima can pose a serious threat to the algorithm's ability to converge to the correct minimum, especially when the first-guess model parameters (particularly the location of the vortex center) contain significant error. Boundary minima in  $J(x_0, y_0)$  can occur near the edge of the analysis domain, and local minima can occur in other multidimensional cross sections of  $J$  because of regions of missing data or deviations of the observed wind pattern from that described by the low-order model. An important special case of such a deviation is the presence of multiple vortices in the data. This local minima problem necessitates the use of multiple first guesses for the location of the vortex and of a two-step approach in which much of the larger-scale flow is retrieved and subtracted before a small-scale vortex retrieval is performed. The latter strategy is necessary in cases where a weaker and broader vortexlike circulation provides a better fit to the low-order model over an analysis domain than a collocated intense

vortex. Finally, the stationarity of the low-order model parameters requires that the temporal analysis domain be limited in order to mitigate violation of the model in cases of rapid flow evolution.

Successful detection and characterization criteria (to be further developed in future work) need to account for nonuniqueness in the vortex parameters due to finite observational resolution and the mathematical nature of the low-order model. One preliminary approach tested herein is the inclusion in the detection criteria of retrieved vortex characteristics that are resolvable on larger scales than the vortex core. This approach demonstrated skill in distinguishing between tornadic and spurious retrieved tornado-like vortices in our experiments with the ARPS simulation and the real dual-Doppler dataset.

Because of computational constraints, it is not possible to apply the technique over the entire multiple-Doppler radar domain in real time. Objective radial velocity criteria were therefore developed to identify subdomains possibly containing tornadoes. These criteria will be further tested and refined through additional tests with real multiple-Doppler tornado observations.

*Acknowledgments.* The authors thank Gordon Carrie for providing the software used to read the DORADE format WSR-88D data used herein. The authors are also grateful to the anonymous referees for their detailed and insightful comments. This work was supported primarily by the Engineering Research Centers Program of the National Science Foundation under NSF Cooperative Agreement EEC-0313747. The ARPS tornado simulation work was supported by NSF Grant ATM-0530814. Any opinions, findings, and conclusions or recommendations expressed in this material are those of the authors and do not necessarily reflect those of the National Science Foundation.

## REFERENCES

- Bluestein, H. B., W.-C. Lee, M. Bell, C. C. Weiss, and A. L. Pazmany, 2003: Mobile Doppler radar observations of a tornado in a supercell near Bassett, Nebraska, on 5 June 1999. Part II: Tornado-vortex structure. *Mon. Wea. Rev.*, **131**, 2968–2984.
- Box, G. E. P., and M. E. Muller, 1958: A note on the generation of random normal deviates. *Ann. Math. Stat.*, **29**, 610–611.
- Brotzge, J., and Coauthors, 2007: CASA IP1: Network operations and initial data. Preprints, *23rd Conf. on IIPS*, San Antonio, TX, Amer. Meteor. Soc., 8A.6. [Available online at <http://ams.confex.com/ams/pdfpapers/120056.pdf>.]
- Crum, T. D., and R. L. Alberty, 1993: The WSR-88D and the WSR-88D operational support facility. *Bull. Amer. Meteor. Soc.*, **74**, 1669–1687.
- Dowell, D. C., C. R. Alexander, J. M. Wurman, and L. Wicker, 2005: Centrifuging of hydrometeors and debris in tornadoes: Radar-reflectivity patterns and wind-measurement errors. *Mon. Wea. Rev.*, **133**, 1501–1524.

- Fletcher, R., and C. M. Reeves, 1964: Function minimization by conjugate-gradients. *Comput. J.*, **7**, 149–153.
- Gal-Chen, T., 1982: Errors in fixed and moving frames of reference: Applications for conventional and Doppler radar analysis. *J. Atmos. Sci.*, **39**, 2279–2300.
- Gao, J.-D., M. Xue, A. Shapiro, and K. K. Droegemeier, 1999: A variational method for the analysis of three-dimensional wind fields from two Doppler radars. *Mon. Wea. Rev.*, **127**, 2128–2142.
- Kapitza, H., 1991: Numerical experiments with the adjoint of a non-hydrostatic mesoscale model. *Mon. Wea. Rev.*, **119**, 2993–3011.
- Lee, W. C., and F. D. Marks, 2000: Tropical cyclone kinematic structure retrieved from single-Doppler radar observations. Part II: The GBVTD-simplex center finding algorithm. *Mon. Wea. Rev.*, **128**, 1925–1936.
- , and J. Wurman, 2005: Diagnosed three-dimensional axisymmetric structure of the Mulhall tornado on 3 May 1999. *J. Atmos. Sci.*, **62**, 2373–2393.
- , F. D. Marks Jr., and R. E. Carbone, 1994: Velocity track display—A technique to extract real-time tropical cyclone circulations using a single airborne Doppler radar. *J. Atmos. Oceanic Technol.*, **11**, 337–356.
- , J.-D. Jou, P.-L. Chang, and S.-M. Deng, 1999: Tropical cyclone kinematic structure retrieved from single Doppler radar observations. Part I: Interpretation of Doppler velocity patterns and the GBVTD technique. *Mon. Wea. Rev.*, **127**, 2419–2439.
- Liou, Y.-C., T.-C. Chen Wang, W.-C. Lee, and Y.-J. Chang, 2006: The retrieval of asymmetric tropical cyclone structures using Doppler radar simulations and observations with the extended GBVTD technique. *Mon. Wea. Rev.*, **134**, 1140–1160.
- Liu, S., M. Xue, and Q. Xu, 2007: Using wavelet analysis to detect tornadoes from Doppler radar radial-velocity observations. *J. Atmos. Oceanic Technol.*, **24**, 344–359.
- Lugt, H. J., 1979: The dilemma of defining a vortex. *Recent Developments in Theoretical and Experimental Fluid Mechanics*, U. Mueller, K. G. Riesner, and B. Schmidt, Eds., Springer-Verlag, 309–321.
- Maddox, R. A., J. Zhang, J. J. Gourley, and K. W. Howard, 2002: Weather radar coverage over the contiguous United States. *Wea. Forecasting*, **17**, 927–934.
- Marzban, C., and G. J. Stumpf, 1996: A neural network for tornado prediction based on Doppler radar-derived attributes. *J. Appl. Meteor.*, **35**, 617–626.
- McLaughlin, D., and Coauthors, 2005: Distributed Collaborative Adaptive Sensing (DCAS) for improved detection, understanding, and predicting of atmospheric hazards. Preprints, *Ninth Symp. on Integrated Observing and Assimilation Systems for the Atmosphere, Oceans, and Land Surface*, San Diego, CA, Amer. Meteor. Soc., P11.3.
- Mitchell, E. D., S. V. Vasiloff, J. G. Stumpf, A. Witt, M. D. Eilts, J. T. Johnson, and K. W. Thomas, 1998: The National Severe Storms Laboratory tornado detection algorithm. *Wea. Forecasting*, **13**, 352–366.
- Moeng, C.-H., and J. C. Wyngaard, 1989: Evaluation of turbulent transport and dissipation closures in second-order modeling. *J. Atmos. Sci.*, **46**, 2311–2330.
- Polak, E., and G. Ribiere, 1969: Note sur la convergence de méthodes de directions conjuguées. *Rev. France Info. Rech. Operationnelle*, **16**, 35–43.
- Rayleigh, L., 1916: On the dynamics of revolving flows. *Proc. Roy. Soc. London*, **A93**, 148–154.
- Roux, F., and F. D. Marks, 1996: Extended velocity track display (EVTD): An improved processing method for Doppler radar observation of tropical cyclones. *J. Atmos. Oceanic Technol.*, **13**, 875–899.
- Shapiro, A., and J. Mewes, 1999: New formulations of dual-Doppler wind analysis. *J. Atmos. Oceanic Technol.*, **16**, 782–792.
- Smith, T. M., and K. L. Elmore, 2004: The use of radial velocity derivatives to diagnose rotation and divergence. Preprints, *11th Conf. on Aviation, Range, and Aerospace*, Hyannis, MA, Amer. Meteor. Soc., P5.6. [Available online at <http://ams.confex.com/ams/pdfpapers/81827.pdf>.]
- Stumpf, J. G., A. Witt, E. D. Mitchell, P. L. Spencer, J. T. Johnson, M. D. Eilts, K. W. Thomas, and D. W. Burgess, 1998: The National Severe Storms Laboratory mesocyclone detection algorithm for the WSR-88D. *Wea. Forecasting*, **13**, 304–326.
- Sun, J., and N. A. Crook, 1994: Wind and thermodynamic retrieval from single-Doppler measurements of a gust front observed during Phoenix II. *Mon. Wea. Rev.*, **122**, 1075–1091.
- , and —, 2001: Real-time low-level wind and temperature analysis using single WSR-88D data. *Wea. Forecasting*, **16**, 117–132.
- , D. W. Flicker, and D. K. Lilly, 1991: Recovery of three-dimensional wind and temperature fields from simulated Doppler radar data. *J. Atmos. Sci.*, **48**, 876–890.
- Wang, Y., T.-Y. Yu, M. Yearly, A. Shapiro, S. Nemati, M. Foster, D. L. Andra Jr., and M. Jain, 2008: Tornado detection using a neuro-fuzzy system to integrate shear and spectral signatures. *J. Atmos. Oceanic Technol.*, **25**, 1136–1148.
- Wang, Z., K. K. Droegemeier, L. White, and I. M. Navon, 1997: Application of a new adjoint Newton algorithm to the 3D ARPS storm-scale model using simulated data. *Mon. Wea. Rev.*, **125**, 2460–2478.
- Wicker, L. J., and R. B. Wilhelmson, 1995: Simulation and analysis of tornado development and decay within a three-dimensional supercell thunderstorm. *J. Atmos. Sci.*, **52**, 2675–2703.
- Wood, V. T., D. C. Dowell, and R. A. Brown, 2004: Simulated WSR-88D measurements of a tornado having a weak reflectivity center. Preprints, *22nd Conf. on Severe Local Storms*, Hyannis, MA, Amer. Meteor. Soc., P7.4. [Available online at <http://ams.confex.com/ams/pdfpapers/81429.pdf>.]
- Wurman, J., and S. Gill, 2000: Finescale radar observations of the Dimmitt, Texas (2 June 1995), tornado. *Mon. Wea. Rev.*, **128**, 2135–2164.
- , and C. R. Alexander, 2005: The 30 May 1998 Spencer, South Dakota, Storm. Part II: Comparison of observed damage and radar-derived winds in the tornadoes. *Mon. Wea. Rev.*, **133**, 97–119.
- , Y. Richardson, C. Alexander, S. Weygandt, and P.-F. Zhang, 2007a: Dual-Doppler and single-Doppler analysis of a tornadic storm undergoing mergers and repeated tornadogenesis. *Mon. Wea. Rev.*, **135**, 736–758.
- , —, —, —, and —, 2007b: Dual-Doppler analysis of winds and vorticity budget terms near a tornado. *Mon. Wea. Rev.*, **135**, 2392–2405.
- Xue, M., and Coauthors, 2001: The Advanced Regional Prediction System (ARPS)—A multi-scale nonhydrostatic atmospheric simulation and prediction tool. Part II: Model physics and applications. *Meteor. Atmos. Phys.*, **76**, 143–165.
- , S. Liu, and T. Yu, 2007: Variational analysis of oversampled dual-Doppler radial velocity data and application to the analysis of tornado circulations. *J. Atmos. Oceanic Technol.*, **24**, 403–414.